applied sciences

MDPI

Article

Study on SPH Viscosity Term Formulations

Xing Zheng [1,*], Qingwei Ma [1,2] and Songdong Shao [1,3]

[1] College of Shipbuilding Engineering, Harbin Engineering University, Harbin 150001, China; q.ma@city.ac.uk (Q.M.); s.shao@sheffield.ac.uk (S.S.)
[2] School of Mathematics, Computer Science and Engineering, City University of London, London EC1V 0HB, UK
[3] State Key Laboratory of Hydraulics and Mountain River Engineering, Sichuan University, Chengdu 610065, China
* Correspondence: zhengxing@hrbeu.edu.cn; Tel.: +86-451-8256-8147

Received: 25 December 2017; Accepted: 1 February 2018; Published: 7 February 2018

Featured Application: The proposed study contributes to the mesh-free numerical modeling field through the examinations of several viscosity term formulations. By simulating benchmark viscosity-dominated flows in engineering practice, the optimal viscosity scheme has been found to work with the Smoothed Particle Hydrodynamics (SPH) method.

Abstract: For viscosity-dominated flows, the viscous effect plays a much more important role. Since the viscosity term in SPH-governing (Smoothed Particle Hydrodynamics) equations involves the discretization of a second-order derivative, its treatment could be much more challenging than that of a first-order derivative, such as the pressure gradient. The present paper summarizes a series of improved methods for modeling the second-order viscosity force term. By using a benchmark patch test, the numerical accuracy and efficiency of different approaches are evaluated under both uniform and non-uniform particle configurations. Then these viscosity force models are used to compute a documented lid-driven cavity flow and its interaction with a cylinder, from which the most recommended viscosity term formulation has been identified.

Keywords: lid-driven flow; second-order derivative; SPH; viscosity domination; viscosity term

1. Introduction

Free surface flow simulations have always generated substantial theoretical and practical interests. Bontozoglou [1] used the spectral spatial discretization method for the laminar film flow along a periodic wall. Scholle et al. [2] used the Finite Element Method (FEM) and complex variable method for modeling the film over corrugated surfaces. Marner et al. [3] developed a potential-velocity formulation of the Navier-Stokes (N-S) equations by using the least square FEM approach. More recently, Marner et al. [4] proposed a generalized complex-valued first integral of the N-S equations for the unsteady Couette flows in a corrugated channel system. Compared with these, the Smoothed Particle Hydrodynamics (SPH) method is equipped with the unique advantage of tracking the free surfaces with much larger deformation even leading to violent breaking.

Since the concept of the mesh-free SPH method was introduced to model hydrodynamic flows [5], SPH has shown its promising performance in a wide range of free surface flows. The benchmark model applications have been documented in the study of dam-break flow [6], wave-structure interaction [7], inflow and outflow [8], porous flow [9] and multi-phase flow [10]. Besides, the shallow water equations (SWEs) were also solved by SPH for the flows in a large area where the vertical flow variations can be reasonably ignored [11,12]. More complex SPH model applications involving the movable bed, sediment and pollutant transport were reported by [13] and Pahar and Dhar [14,15]. Besides, some recent weakly compressible SPH (WCSPH) works include a robust procedure to filter the

high-frequency oscillations in the pressure field arising from the use of the artificial sound speed, in the field of both strong dynamics [16] and slow dynamics [17]. These were based on the improvement of certain diffusive approaches (e.g., [18]) in which the numerical noise was just alleviated through the additional post-processing of the pressure data.

The above-mentioned free surface flows are dominated by the gravity and pressure influence. To improve the modeling accuracy of such flows, quite a few studies have been done to enhance the SPH pressure formulation [19] and the pressure solution in either the WCSPH [20] or incompressible SPH (ISPH) [21]. On the other hand, there is another kind of the flow, which is also of great engineering interest, but dominated by the influence of the flow viscosity, such as a lid-driven cavity flow. To realistically simulate these, the treatment of the viscosity force term in the N-S equations becomes important. As compared with the established studies on the pressure formulation, the research on the viscosity term was paid much less attention in the SPH field, probably due to its minor role in the medium-to-high Reynolds number flows commonly found in the free surface applications. Besides, one technical difficulty arises from the fact that the viscosity term involves a second-order derivative calculation, while the pressure term is only of the first-order, and therefore the numerical treatment becomes more complex.

The earliest viscosity term treatment in SPH adopted the artificial viscosity approach proposed by Monaghan [5] to avoid the particle instability and thus to maintain the computational stability. The effect of relevant parameters in the artificial formulation was extensively explored by De Padova et al. [22] in their SPH simulation of six different regular waves. Following the establishment of the projection SPH [23] and ISPH [24], the real viscosity term form based on Morris et al. [25] has been more widely used. Compared with the artificial viscosity, the real viscosity has a clearer physical implication and it also performs much better in the practical SPH applications. To improve viscosity performance in reproducing the broken free surfaces, Khayyer et al. [26] made one step-forward correction by comprehensively addressing the linear and angular momentum conservations. In a turbulent flow where the particle resolution is insufficient, an eddy viscosity term has been proposed by Gotoh et al. [27] using the sub-particle-scale (SPS) shear stress model. Recently, quite a few viscosity corrections were reported to show their importance in viscosity-dominated flow applications. For example, Basa et al. [28] reviewed the early viscosity formulations for a wide range of Reynolds numbers using a Poiseuille channel and lid-driven cavity flow. Colagrossi et al. [29] used three viscosity models to investigate the consistency and energy mechanisms of the SPH scheme. Grenier et al. [30] adopted the renormalized Morris et al. formulation with an inter-particle dynamic viscosity coefficient to model the merging process of two viscous bubbles. The latest work in the field could be attributed to Liu and Liu [31], who studied the viscous forces in a Poiseuille flow on both the regular and irregular particle configurations.

Quite a few established approaches treat the real viscosity term by using a hybrid formulation of the SPH first-order derivative combined with a finite difference representation. However, the viscosity term appears in the N-S equations as a second-order derivative. A more refined treatment of this should greatly improve the SPH performance in viscosity-dominated flows. In a recent review work, Ma et al. [32] comprehensively summarized all existing formulations of the Laplacian term used in the pressure Poisson equation (PPE) of ISPH models. Laplacian is a second-order derivative representation, which is basically similar to the viscosity term. Thus, the present study aims to model the viscosity term by following similar treatment algorithms used in the Laplacian formulation and then further examine the new model performance.

The paper is structured as follows. The next chapter briefly reviews the ISPH methodology. Then a review on several second-order derivative approximations used in the PPE is made and the associated discretization schemes are transformed to model the viscosity term. After this a detailed benchmark patch test based on a polynomial function is carried out to evaluate the accuracy and efficiency of different viscosity force models, under both the regular and irregular particle configurations. Finally, two viscosity-dominated flows are used to further demonstrate the importance of the viscosity term

effect in practical model applications, including the lid-driven cavity flow and its interaction with an inside cylinder.

2. Materials and Methods I—General ISPH Methodology

The basic concept of SPH is that a particle is fundamental in the Lagrangian description and the motion of a continuum can be represented with high accuracy by simulating the motion of a large number of such particles. Through the use of the integral interpolants, any field variables can be expressed by the integrals that are approximated by the summation interpolants over the neighboring particles. Similarly, the spatial derivatives at each particle location can also be evaluated by the summation interpolants. The derivatives are computed based on the kernel function, which can be obtained analytically. For example, the particle approximation of a value $f(\mathbf{r}_i)$ and its gradient $\nabla f(\mathbf{r}_i)$ can be shown as

$$f(\mathbf{r}_i) = \sum_{j=1}^{N} \frac{m_j}{\rho_j} f(\mathbf{r}_j) W(\mathbf{r}_i - \mathbf{r}_j, h_i) \tag{1}$$

$$\nabla f(\mathbf{r}_i) = \sum_{j=1}^{N} \frac{m_j}{\rho_j} f(\mathbf{r}_j) \nabla_i W(\mathbf{r}_i - \mathbf{r}_j, h_i) \tag{2}$$

where i is the reference particle and j represents all the neighboring particles; N is the number of particles for the summation; m_j is the particle mass; ρ_j is the particle density; $\mathbf{r}_i$ and $\mathbf{r}_j$ are the positions of the particle; W is the SPH interpolation kernel function; $\nabla_i W$ represents the gradient of the kernel taken with respect to the reference particle; and h is the kernel smoothing length. The kernel function can have many different forms and a cubic spline kernel is used in this paper due to its computational accuracy and efficiency. In a practical SPH computation, the gradient of the pressure P and divergence of the velocity $\mathbf{u}$ are usually calculated by

$$\nabla P_i = \rho_i \sum_{j=1}^{N} m_j \left(\frac{P_j}{\rho_j^2} + \frac{P_i}{\rho_i^2} \right) \nabla_i W(\mathbf{r}_i - \mathbf{r}_j, h_i) \tag{3}$$

$$\nabla \cdot \mathbf{u}_i = -\frac{1}{\rho_i} \sum_{i=1}^{N} m_j \mathbf{u}_{ij} \cdot \nabla_i W(\mathbf{r}_i - \mathbf{r}_j, h_i) \tag{4}$$

where $\mathbf{u}_{ij} = \mathbf{u}_i - \mathbf{u}_j$ is defined as the velocity difference.

In an ISPH approach the fluid density is assumed to be constant. Therefore, the mass and momentum conservation equations, i.e., N-S equations, can be written in the following quasi-Lagrangian description as

$$\nabla \cdot \mathbf{u} = 0 \tag{5}$$

$$\frac{D\mathbf{u}}{Dt} = -\frac{1}{\rho} \nabla P + \mathbf{g} + \nu_0 \nabla^2 \mathbf{u} \tag{6}$$

where t is the time; $\mathbf{g}$ is the gravitational acceleration; and ν_0 is the kinematic viscosity.

The two-step projection method [24] is used to solve the velocity and pressure in Equations (5) and (6). The first step is the prediction of velocity in the time domain without including the pressure term. The intermediate particle velocity and position are obtained as

$$\mathbf{u}_* = \mathbf{u}_t + \Delta \mathbf{u}_* \tag{7}$$

$$\Delta \mathbf{u}_* = \left(\mathbf{g} + \nu_0 \nabla^2 \mathbf{u} \right) \Delta t \tag{8}$$

$$\mathbf{r}_* = \mathbf{r}_t + \mathbf{u}_* \Delta t \tag{9}$$

where $\mathbf{u}_t$ and $\mathbf{r}_t$ are the velocity and position of particle at time t; Δt is the time step; $\Delta \mathbf{u}_*$ is the velocity change; and $\mathbf{u}_*$ and $\mathbf{r}_*$ are the intermediate velocity and position of particle.

In the second step the pressure term is used, leading to a correction of the particle velocity $\Delta \mathbf{u}_{**}$ as

$$\Delta \mathbf{u}_{**} = -\frac{1}{\rho} \nabla P_{t+\Delta t} \Delta t \tag{10}$$

Then the new time-step values are updated by

$$\mathbf{u}_{t+\Delta t} = \mathbf{u}_{*} + \Delta \mathbf{u}_{**} \tag{11}$$

$$\mathbf{r}_{t+\Delta t} = \mathbf{r}_{t} + \frac{\mathbf{u}_{t} + \mathbf{u}_{t+\Delta t}}{2} \Delta t \tag{12}$$

where $\mathbf{u}_{t+\Delta t}$ and $\mathbf{r}_{t+\Delta t}$ are the velocity and position of the particle at new time step.

According to Zheng et al. [33], the following form of the pressure Poisson equation, which includes the divergence of flow velocity and the variance of particle density as the mixed source term, is used to solve the fluid pressure for enhancing the model performance. This equation was derived from the combination of the continuity equation (Equation (5)) and the velocity correction (Equation (10)), based on the compressible form of the continuity equation $D\rho/Dt = \rho \nabla \cdot \mathbf{u}$.

$$\nabla^2 P_{t+\Delta t} = \alpha \frac{\rho - \rho^*}{\Delta t^2} + (\alpha - 1) \frac{\rho \nabla \cdot \mathbf{u}_{*}}{\Delta t} \tag{13}$$

where α is a weighting coefficient and a value of 0.01 is used from the computational experiences.

The left-hand-side of Equation (13), i.e., the Laplacian term, is commonly discretized by merging the standard SPH gradient formulation with a first-order finite difference scheme as

$$\nabla \cdot \left(\frac{1}{\rho^*} \nabla P_{t+1} \right) = \sum_{j=1}^{N} m_j \frac{8}{\left(\rho_i + \rho_j \right)^2} \frac{P_{ij} \mathbf{r}_{ij}}{{\mathbf{r}_{ij}}^2 + \eta^2} \cdot \nabla_i W\left(\mathbf{r}_i - \mathbf{r}_j, h \right) \tag{14}$$

where $P_{ij} = P_i - P_j$ is defined as the pressure difference and $\mathbf{r}_{ij} = \mathbf{r}_i - \mathbf{r}_j$ the position difference; and η is a small number to avoid singularity.

In the present ISPH model, the kinematic free surface boundary conditions can be automatically satisfied due to the mesh-free nature of the model. The free surface particles are identified by using the auxiliary functions combined with the particle number density criterion by following Zheng et al. [33]. Besides, to improve the treatment of the solid boundary conditions, a high accuracy of the Simplified Finite Difference Interpolation (SFDI) scheme is used on the solid walls to solve the PPE. One promising feature of this pressure solution scheme is that the normal pressure gradient is computed on the solid boundary without the use of the mirror particles. This can improve the simulation accuracy near the solid wall, and meanwhile reduce the CPU cost.

In a viscous flow, the dynamic boundary condition should be an exact equilibrium between the pressure, viscous stress and surface tension, as pointed out by Scholle et al. [2]. Since there is no free surface involved in the present model applications, a simple approximation based on the zero pressure only is imposed as the dynamic free surface boundary condition.

3. Materials and Methods II—SPH Viscosity Term Formulations

Ma et al. [32] comprehensively reviewed the established SPH discretization schemes for the second-order Laplacian term in the PPE. In this section, four representative formulations are selected to model the viscosity term as below.

3.1. Hybrid Form Viscosity Force Model-01 (VISC-01)

This was proposed by Cummins and Rudman [23] by using a hybrid of the standard SPH gradient formulation combined with a first-order finite difference scheme. It can also be obtained through the

analysis of the viscous stress such as documented by Morris et al. [25]. Shao and Lo [24] adopted this form in their ISPH model. This kind of the viscosity term representation is usually written as

$$\nabla^2 \mathbf{u}^\alpha = 2\sum_{j=1}^{N} \frac{m_j}{\rho_j} \frac{\mathbf{u}_{ij}^\alpha \mathbf{r}_{ij}}{\mathbf{r}_{ij}{}^2 + \eta^2} \cdot \nabla_i W(\mathbf{r}_i - \mathbf{r}_j, h) \tag{15}$$

where α indicates the spatial component.

3.2. Direct Form Viscosity Force Model-02 (VISC-02)

Originally aiming to improve the accuracy of Laplacian approximation, Gotoh et al. [34] derived a new form of the equations by directly taking the divergence of a SPH gradient model. This was actually founded on the twice differentiation of the SPH interpolant, and therefore it intrinsically contains the second-derivative of a kernel. By adopting a similar approach of the derivation, the viscosity term can be modeled as

$$\nabla^2 \mathbf{u}^\alpha = \sum_{j=1}^{N} \frac{m_j}{\rho_j} \mathbf{u}_{ij}^\alpha \left(\frac{\partial^2 W_{ij}}{\partial r_{ij}^2} - \frac{1}{\mathbf{r}_{ij}} \frac{\partial W_{ij}}{\partial r_{ij}} \right) \tag{16}$$

However, as pointed out by Gotoh et al. [34], this formulation is very sensitive to the particle disorder, especially when the order of the kernel function is low.

3.3. Schwaiger Form Viscosity Force Model-03 (VISC-03)

Schwaiger [35] proposed a higher-order derivation approach, which is based on the gradient approximations used in the thermal, viscous and pressure projection problems, but including the higher-order terms in appropriate Taylor series. By substituting the pressure variable in the original formulation of Schwaiger [35] with the flow velocity, the following viscosity representation can be obtained

$$\nabla^2 \mathbf{u}^\alpha = \frac{\mathbf{H}_{\beta\beta}^{-1}}{\kappa} \{ 2\sum_{j=1}^{N} \frac{m_j}{\rho_j} \frac{\mathbf{u}_{ij}^\alpha \mathbf{r}_{ij}}{\mathbf{r}_{ij}{}^2 + \eta^2} \cdot \nabla_i W(\mathbf{r}_i - \mathbf{r}_j, h) - 2\nabla \mathbf{u}_i^\alpha \cdot \sum_{j=1}^{N} \frac{m_j}{\rho_j} \nabla_i W(\mathbf{r}_i - \mathbf{r}_j, h) \} \tag{17}$$

$$\nabla \mathbf{u}_i^\alpha = \sum_{j=1}^{N} (\mathbf{u}_j^\alpha - \mathbf{u}_i^\alpha) \mathbf{\Gamma}_{ij} \nabla W \tag{18}$$

$$\mathbf{\Gamma}_{ij} = \begin{bmatrix} \sum \frac{m_j}{\rho_j} (x_j - x_i) \frac{\partial W_{ij}}{\partial x} & \sum \frac{m_j}{\rho_j} (y_j - y_i) \frac{\partial W_{ij}}{\partial x} \\ \sum \frac{m_j}{\rho_j} (x_j - x_i) \frac{\partial W_{ij}}{\partial y} & \sum \frac{m_j}{\rho_j} (y_j - y_i) \frac{\partial W_{ij}}{\partial y} \end{bmatrix}^{-1} \tag{19}$$

where κ is the number of dimensions; and $\mathbf{H}_{\beta\beta} = \int_\Omega \frac{m_j}{\rho_j} \frac{(\mathbf{r}_{ij})_\alpha W_{,\alpha}}{|\mathbf{r}_{ij}|^2} (\mathbf{r}_{ij})_\beta (\mathbf{r}_{ij})_\beta$ is defined. The size of $\mathbf{H}_{\beta\beta}^{-1}$ and $\mathbf{\Gamma}_{ij}$ is 2×2 in a 2D and 3×3 in a 3D application. Schwaiger's approach requires the inverse operations of the matrices $\mathbf{H}_{\beta\beta}^{-1}$ and $\mathbf{\Gamma}_{ij}$ at each fluid particle, so it could cost a little more in computational expenses. The original formulation was developed for the thermal diffusion solutions, and Jian et al. [36] used this for the fluid-structure interactions in their ISPH approach.

3.4. Oger, Hosseini and Feng, Khayyer Form Viscosity Force Model-04 (VISC-04)

Oger et al. [37] studied a wide range of the correction procedures to improve the accuracy of kernel approximations and they proposed a renormalization technique from the discrete version of the Eulerian equations. Based on the study, they eventually constructed a correction matrix to account for

the irregular distribution of the neighboring particles around the reference one. This is written in the form of the viscosity term representation as

$$\nabla^2 \mathbf{u}^{\alpha} = 2\sum_{j=1}^{N} \frac{m_j}{\rho_j} \frac{\mathbf{u}_{ij}^{\alpha} \mathbf{r}_{ij}}{\mathbf{r}_{ij}{}^2 + \eta^2} \boldsymbol{\Gamma}_{ij} \nabla W(\mathbf{r}_i - \mathbf{r}_j, h) \tag{20}$$

where the correction matrix $\boldsymbol{\Gamma}_{ij}$ has the same form as Equation (19) for a 2D problem, while it becomes a 3×3 matrix in 3D. It should be noted that in a follow-on study, Hosseini and Feng [38] refined this approximation to ensure the gradient function being accurately calculated. Also Khayyer et al. [26] developed a similar correction technique on the kernel gradient to calculate the viscous forces, therefore both the linear and the angular momentums are exactly conserved in their ISPH model.

4. Results I—Analysis of Model Accuracy through Benchmark Tests

In this section, the detailed numerical investigations are made into the convergence and accuracy behaviors of the above four viscosity force models, under both the uniform and random particle distributions in a 2D framework. The error of the numerical result is quantified as

$$Err = \frac{1}{M} \sum_{j=1}^{M} \left| \frac{\nabla^2 \widetilde{f}(\mathbf{x}_j) - \nabla^2 f(\mathbf{x}_j)}{\nabla^2 \widetilde{f}(\mathbf{x}_j)} \right| \tag{21}$$

where Err is the mean numerical error; $\nabla^2 \widetilde{f}(\mathbf{x}_j)$ is the numerical value; $\nabla^2 f(\mathbf{x}_j)$ is the analytical solution; and M is the number of sampling points in the whole domain.

The computational domain of the test is chosen as a square with the side length of 1 m as shown in Figure 1. The test function uses a polynomial of second-order expressed by $f(x, y) = x^4 + y^4$. The SPH kernel function used is a cubic spline kernel [5] normalized in 2D. The SPH particles are arranged in a uniform and non-uniform configuration, respectively. In the former case a uniform Cartesian configuration of the particles is used, while in the latter case the particle positions are determined by $\widetilde{\mathbf{r}} = \mathbf{r} + (Rn - 0.5)\Delta\mathbf{r}$, where Rn is a random number with a value (0, 1) through the quasi-random number generator, and $\Delta\mathbf{r}$ is the particle size vector in 2D under the uniform distribution condition. A sample particle distribution is also illustrated in Figure 1 for the particle number of 400. In the following test, five different particle resolutions are considered, including a total number of 20×20, 40×40, 60×60, 80×80, 100×100 particles. This corresponds to the particle size of dx = 0.05 m, 0.025 m, 0.01667 m, 0.0125 m and 0.01 m, respectively.

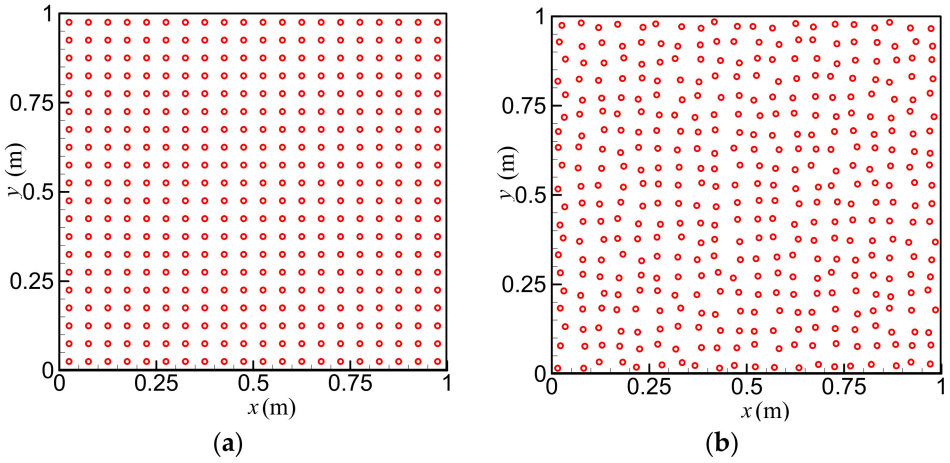

Figure 1. Particle distributions with the particle number of 400: (**a**) under uniform distribution; and (**b**) under non-uniform distribution.

4.1. Accuracy under Uniform Distribution of the Particles

To examine the second-order derivative of the polynomial function, i.e., $\Delta f(x,y) = \nabla^2 f = 12(x^2 + y^2)$, Figure 2 gives the comparisons between the analytical and numerical results computed by the different SPH viscosity force models, at x = 0.5 m and y = (0, 1) m, under uniform particle distribution with a particle size dx = 0.05 m. As shown in Figure 2, all the four viscosity methods led to a very good agreement with the analytical results when the particles are uniformly distributed.

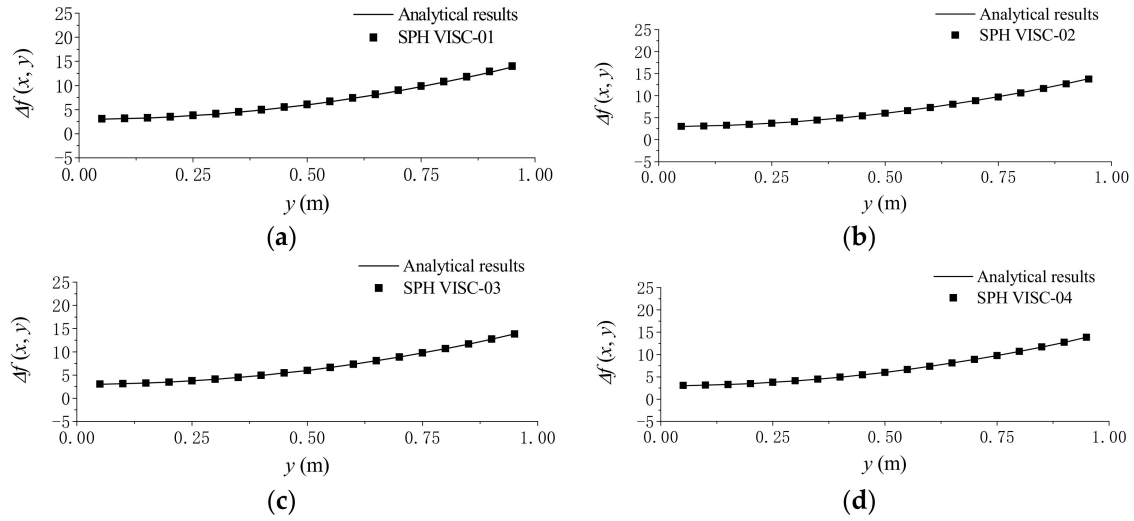

Figure 2. Comparisons of analytical and numerical results computed by using different viscosity force models with the uniform particle distribution: (**a**) VISC-01; (**b**) VISC-02; (**c**) VISC-03; and (**d**) VISC-04. SPH, Smoothed Particle Hydrodynamics; VISC, Viscosity Force Model.

As a sensitivity test, Table 1 gives the mean errors defined by Equation (21) for the different particle numbers computed by the four different viscosity force models. Figure 3 further gives the convergence rate in the form of the total particle number N and the numerical error Err, in which k refers to the convergence ratio. That is to say, k = 1 indicates the numerical model can achieve the first-order convergence, while k = 2 the second-order convergence. Both Table 1 and Figure 3 are provided based on the uniform particle distributions. According to Table 1, the accuracy of VISC-01 is the lowest, while VISC-03 and VISC-04 can achieve the highest accuracy, and VISC-02 lies somewhere in the between. This conclusion is further consolidated by Figure 3, which clearly shows the convergence rate of each viscosity force model. It is well indicated that VISC-01 and VISC-02 are around the first-order accuracy, while VISC-03 and VISC-04 can obtain the second-order.

Table 1. Mean errors with different particle numbers and viscosity calculation methods under the uniform particle distribution. VISC, Viscosity Force Model.

Particle No.	VISC-01	VISC-02	VISC-03	VISC-04
20 × 20	5.00×10^{-5}	1.68×10^{-5}	4.65×10^{-6}	4.65×10^{-6}
40 × 40	9.81×10^{-6}	4.24×10^{-6}	2.37×10^{-7}	2.37×10^{-7}
60 × 60	4.08×10^{-6}	1.84×10^{-6}	4.38×10^{-8}	4.38×10^{-8}
80 × 80	2.22×10^{-6}	1.02×10^{-6}	1.34×10^{-8}	1.34×10^{-8}
100 × 100	1.40×10^{-6}	6.45×10^{-6}	5.39×10^{-9}	5.39×10^{-9}

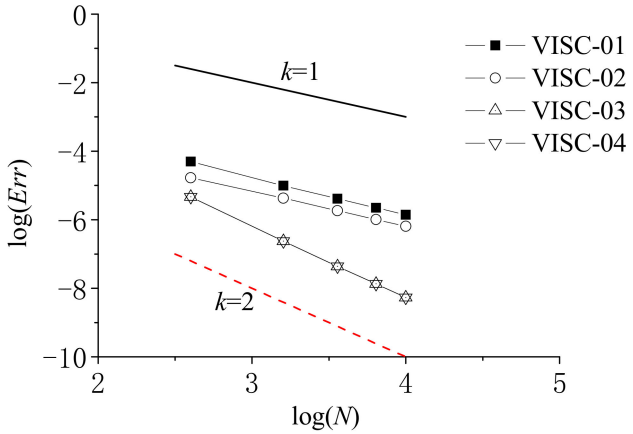

Figure 3. Convergence and error analysis of different viscosity force models under the uniform particle distribution.

4.2. Accuracy under Non-Uniform Distribution of the Particles

For the non-uniform particle distributions, Figure 4 gives the comparisons of the analytical and numerical results computed by using four different viscosity force models. In this case, x is around $(0.5 - 0.1\ dx, 0.5 + 0.1\ dx)$ m and y still ranges within (0, 1) m. The particles are irregularly distributed within the domain and the initial particle size is $dx = 0.05$ m. According to the results shown in Figure 4, VISC-03 can achieve the most accurate result, while the errors of VISC-01 and VISC-04 are the highest. This situation is completely different from the uniform particle distribution, as shown in Figure 2.

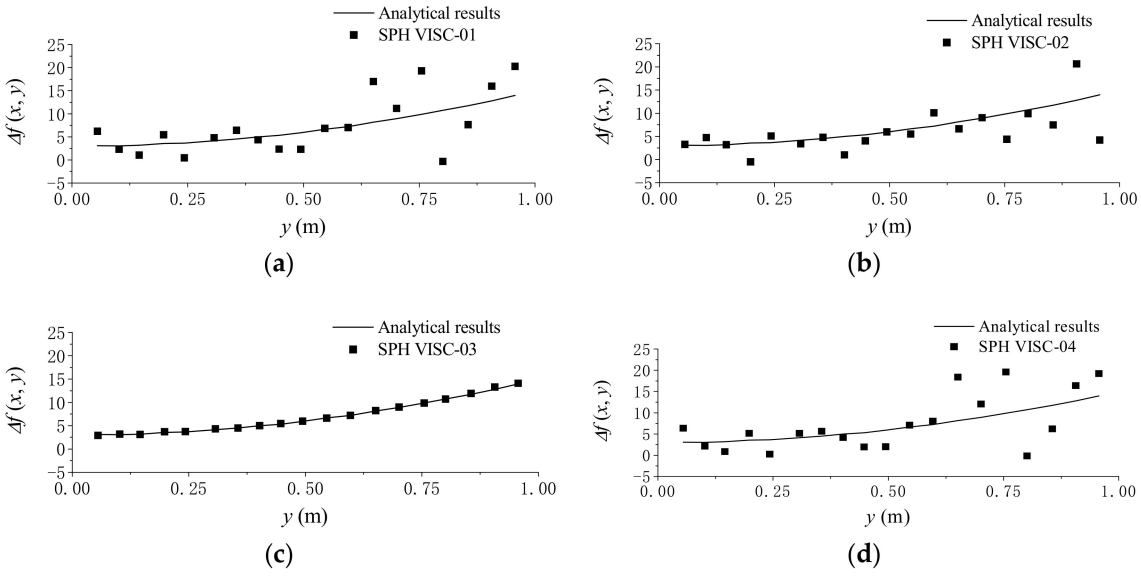

Figure 4. Comparisons of analytical and numerical results computed by using different viscosity force models with the non-uniform particle distribution: (**a**) VISC-01; (**b**) VISC-02; (**c**) VISC-03; and (**d**) VISC-04.

Furthermore, Table 2 gives the mean errors for the different particle numbers computed by the different viscosity methods, and Figure 5 gives the convergence rate corresponding to the particle number N and error Err, under the non-uniform particle configurations. From Table 2, the results of VISC-03 show the best accuracy, while VISC-01 and VISC-04 results demonstrate the least satisfactory performance. In comparison, VISC-02 results are in the middle range. Also, it can be found that the

errors of VISC-04 change a lot with the different particle numbers. Besides, Figure 5 quantitatively shows that the convergence rate of VISC-03 is near the first-order accuracy, while the other three models cannot reach this level of the convergence. Similar results are also observed on VISC-01 and VISC-04.

Table 2. Mean errors with different particle numbers and viscosity calculation methods under the non-uniform particle distribution.

Particle No.	VISC-01	VISC-02	VISC-03	VISC-04
20 × 20	2.79×10^{-3}	1.32×10^{-3}	5.62×10^{-5}	2.84×10^{-3}
40 × 40	1.25×10^{-3}	5.85×10^{-4}	1.18×10^{-5}	1.28×10^{-3}
60 × 60	8.41×10^{-4}	3.80×10^{-4}	5.25×10^{-6}	8.68×10^{-4}
80 × 80	6.04×10^{-4}	2.94×10^{-4}	2.90×10^{-6}	6.20×10^{-4}
100 × 100	4.72×10^{-4}	2.27×10^{-4}	1.82×10^{-6}	4.85×10^{-4}

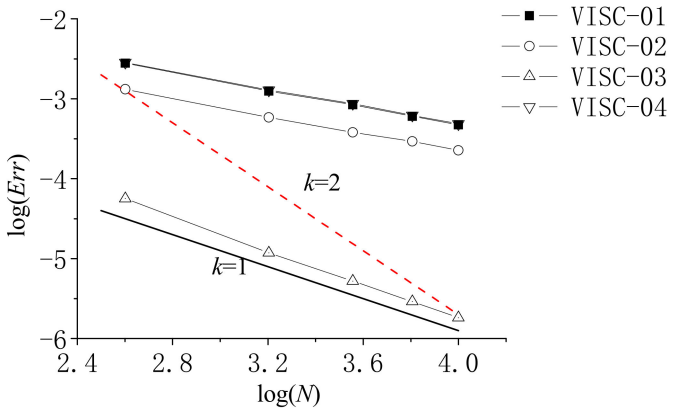

Figure 5. Convergence and error analysis of different viscosity force models under the non-uniform particle distribution.

4.3. Analysis of CPU Expenses

To show the CPU efficiency of different viscosity methods, Table 3 gives the comparisons of CPU time corresponding to the different particle numbers and viscosity force models, when the particles are under the irregular distribution. For the present benchmark patch test, the CPU time under the regular distribution of the particles is nearly the same as that under the irregular distribution. It shows that the CPU cost of VISC-02 is the cheapest, while that of VISC-03 is the heaviest. In contrast, the CPU time of VISC-01 is a little longer than that of VISC-02, but it is much shorter than that of VISC-04. Figure 6 provides the convergence analysis of each viscosity force model in view of the CPU time, in which a unanimously first-order convergence rate is found among the four models.

Table 3. Comparisons of CPU time with different particle numbers and viscosity calculation methods under the non-uniform particle distribution (unit: s).

Particle No.	VISC-01	VISC-02	VISC-03	VISC-04
20 × 20	0.089	0.074	0.204	0.179
40 × 40	0.382	0.307	0.850	0.741
60 × 60	0.900	0.739	1.976	1.719
80 × 80	1.526	1.269	3.500	3.024
100 × 100	2.444	1.987	5.493	4.722

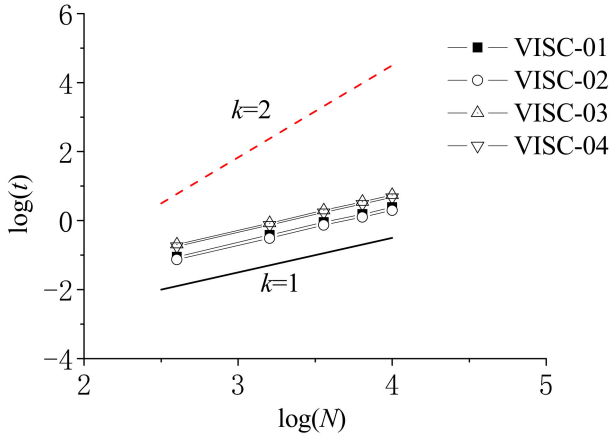

Figure 6. Convergence analysis of CPU time for different viscosity force models under the non-uniform particle distribution.

4.4. Brief Evaluations of Four Viscosity Force Models

Based on the above accuracy and efficiency analysis, it shows that VISC-03 can attain the highest accuracy under either the uniform or non-uniform particle distributions. In comparison, VISC-04 can achieve the similar accuracy but only under the uniform particle distributions, while its accuracy degrades to that of VISC-01 when the particles are randomly distributed. Among these the accuracy of VISC-02 lies in somewhere in-between. However, in view of the CPU efficiency, VISC-02 is the fastest model but VISC-03 is the slowest. To further examine different viscosity force models in a practical ISPH simulation, more benchmark test cases will be studied in the next section.

Besides, it has also been found that the mean errors obtained by VISC-03 and VISC-04 are always the same in case of the uniform particle distribution while significant differences occur for the non-uniform distribution. This is due to the fact that, under the uniform distribution of the particles, the second term on the right-hand-side of Equation (17) becomes zero, and also $H_{\beta\beta}^{-1}/\kappa$ becomes unity. Therefore, Equations (17) and (20) become exactly identical, leading to the same performance of VISC-03 and VISC-04. On the other hand, these conditions do not hold under the non-uniform particle distribution, and the numerical differences become significantly larger as a result.

5. Results II—Model Application in Practical Viscous Flows

In order to demonstrate the effect of four methods of viscosity term calculation, this section presents two numerical tests on the viscous flow modeling, which are based on the benchmarks of the lid-driven flow and its interaction with an inside cylinder. This would provide more useful information on the different viscosity force models in practical situation. The lid-driven flows have been widely used as a benchmark validation case for the different SPH viscosity force models. For example, Zheng et al. [33] used an artificial viscosity, Leroy et al. [39] used a turbulent dynamic viscosity, Aly et al. [40] used a Morris formula, and Yildiz et al. [41] derived a more general second-order derivative approximation based on the Taylor series expansion and the concept of second- and fourth-order isotropic tensors.

5.1. Lid-Driven Flow

A lid-driven flow within a 2D square cavity of height H and width L is considered in the present section. The two side walls and the bottom wall of the cavity are stationary, while the top wall experiences a constant forced motion. The velocity of the top wall in the x-direction is given by U_0. In the numerical study, the following parameters are used: $H = L = 1.0$ m, kinematic viscosity $\nu = 0.001$ m^2/s, and $\mathrm{Re} = U_0 L/\nu$, where $U_0 = 1.0$ m/s is adopted.

Figure 7 gives the vector plots of lid-driven flow forced by the uniform motion of the top lid for the Reynolds number Re = 1000, with two different particle numbers of N = 1600 and 10,000, respectively. The computational time step Δt = 0.001 s is used. The simulation was carried out until t = 40 s when the velocity distribution reached the stable state. To validate the numerical results, Figure 8 gives the comparisons on the velocity amplitude distribution computed by the OpenFOAM (i.e., Open source Field Operation and Manipulation, [42]) and ISPH (VISC-04), in which a similar velocity field has been found from the two model results.

OpenFOAM is a C++ toolbox for the development of customized numerical solvers, and pre-/post-processing utilities for the solution of continuum mechanics including CFD problems. OpenFOAM uses the finite volume method (FVM) and is a typically mesh-based numerical model. The FVM uses a co-located methodology on an unstructured grid with arbitrary grid element. A variety of available interpolation, discretization and matrix solution schemes can be selected at runtime and both the implicit and explicit solution techniques are accessible to the end-users.

In order to quantify the accuracy of different viscosity calculation methods, Figure 9 gives the comparisons of velocity component distributions ux at x = 0.5 m and uy at y = 0.5 m with the experimental data of Ghia et al. [43] and OpenFOAM. In this case, the following computational parameters are used: particle size dx = 0.005 m, simulation time t = 40 s and Reynolds number Re = 1000. It is shown from Figure 9 that the results obtained by the four viscosity calculation methods are generally quite similar to each other. By examining the enlarged chart where the velocity experiences a larger gradient, however, it can be found that the results obtained by VISC-04 can get the best agreement with the experimental data.

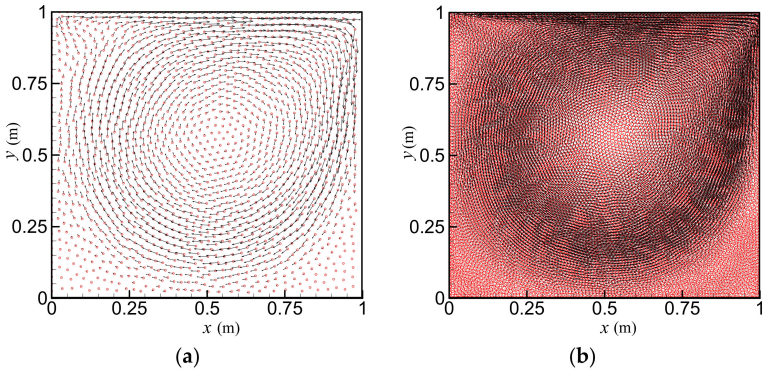

Figure 7. Vector plots of lid-driven flow for the two different particle numbers: (**a**) N = 1600; and (**b**) N = 10,000. Red, location of fluid particle; Black, velocity of flow field.

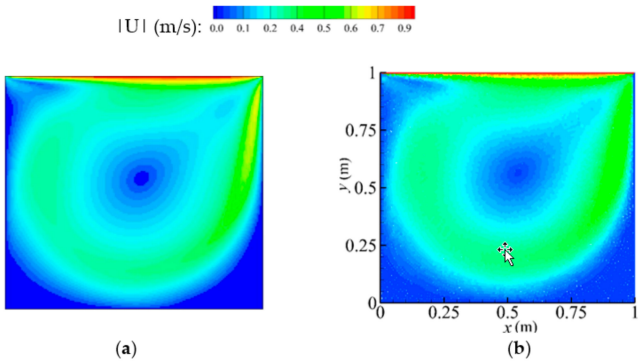

Figure 8. Velocity amplitude patterns of the lid-driven flow computed by (**a**) OpenFOAM; and (**b**) ISPH (VISC-04).

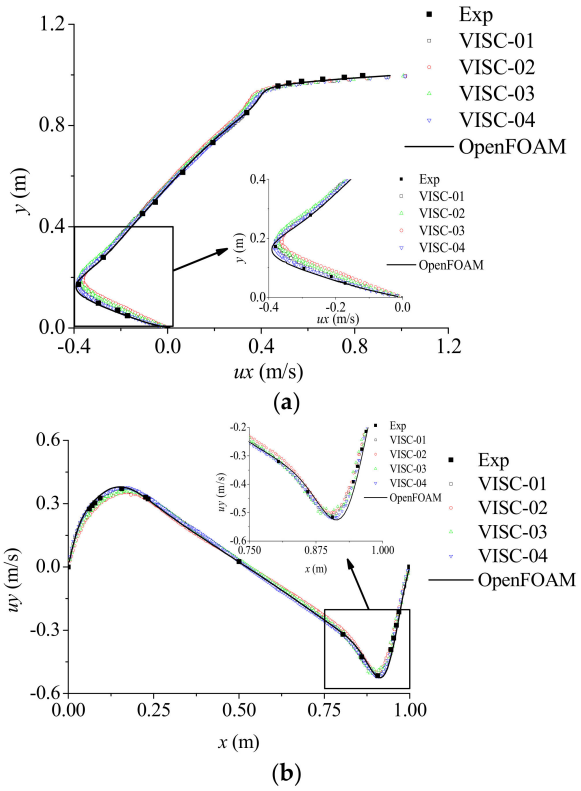

Figure 9. Comparisons of four viscosity force models for the lid-driven flow: (**a**) ux velocity distribution; and (**b**) uy velocity distribution. OpenFOAM, Open source Field Operation and Manipulation; Exp, Experimental data of Ghia et al.

Furthermore, for the purpose of model convergence analysis, Figure 10 gives the errors in minimum ux value between the experimental data and various ISPH results for the different particle resolutions. The computational results of OpenFOAM are also shown for a comparison. The numerical error is defined by $Err=|ux_{\min,n} - ux_{\min,e}|$, where $ux_{\min,n}$ is the numerical minimum and $ux_{\min,e}$ is the experimental one. According to the results in Figure 10, all errors obtained by the ISPH viscosity force models unanimously show a decreasing trend with a decrease in the particle size, i.e., an increase in the particle number. Meanwhile, VISC-04 can achieve the smallest errors among all viscosity force models under the same particle scale.

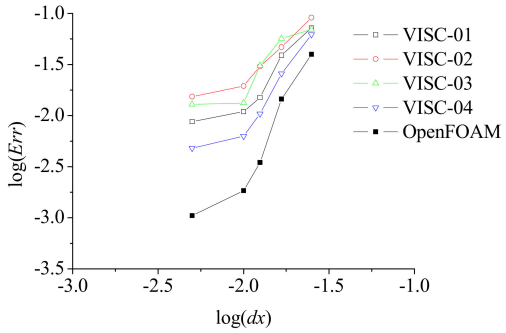

Figure 10. Convergence and error analysis of four viscosity force models for the different particle resolutions of a lid-driven flow.

5.2. Lid-Driven Flow with an Inside Cylinder

To provide a further robust evaluation on the proposed ISPH viscosity force models, this section explores a more complex lid-driven flow case with a cylinder inside. The schematic set up of the model is shown in Figure 11a. There is a cylinder inside the cavity region, with its diameter being $d = 0.5\ L$. The 2D square cavity has a height H and width L, with the dimensions of $H = L = 1.0$ m. The center of the cylinder is located at $(0.5\ L, 0.5\ H)$. The wall boundary of both the cylinder and the cavity region is set as the non-slip and non-penetration condition in the tangential and normal directions, respectively, where u_r and u_n indicate the velocity component in each direction. The velocity of the top wall of the cavity in the x-direction is given by $U_0 = 1.0$ m/s, which leads to a Reynolds number $Re = 1000$. The other computational parameters are kept unchanged as those used in Section 5.1. Based on the ISPH model simulations (with VISC-04), Figure 11b gives the result of velocity vector plots of the cavity flow at particle number $N = 10{,}000$ and simulation time $t = 40$ s, when the steady results are achieved. Figure 12 shows the comparison of velocity amplitude patterns between the ISPH and OpenFOAM computations, and a qualitatively good agreement has been found.

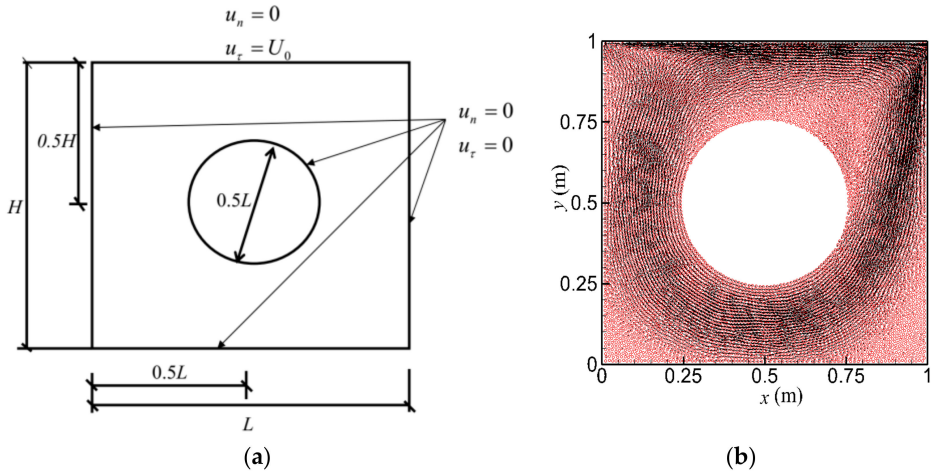

Figure 11. (**a**) Schematic setup of the lid-driven flow model with a cylinder inside; and (**b**) Velocity vector plot of the cavity flow at time $t = 40$ s. Red, location of fluid particle; Black, velocity of flow field.

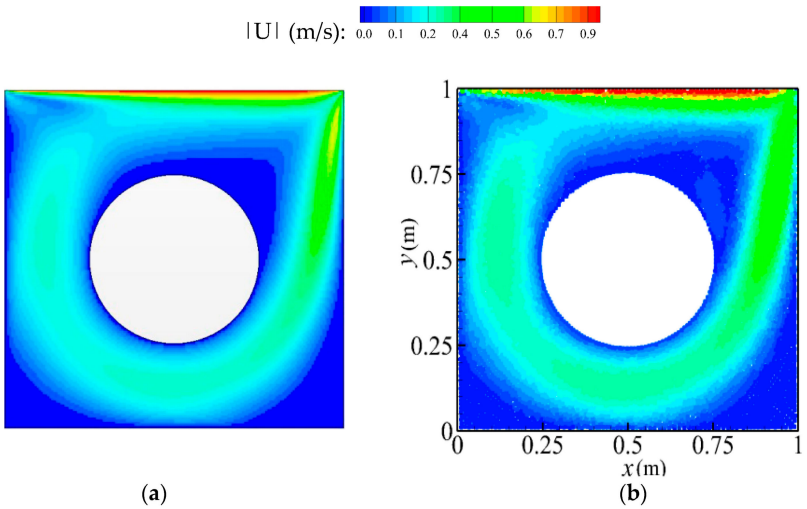

Figure 12. Velocity amplitude patterns of the lid-driven flow with an inside cylinder computed by: (**a**) OpenFOAM; and (**b**) ISPH (VISC-04).

To finally examine the performance of different viscosity force models, Figure 13 gives the comparisons of velocity *ux* distributions at $x = 0.5$ m and *uy* distributions at $y = 0.5$ m, computed by the ISPHs and FVM-based OpenFOAM. In this case, the computational parameters are: particle size $dx = 0.005$ m, time $t = 40$ s and Reynolds number $Re = 1000$. As shown in Figure 13, the results obtained by the four viscosity calculation methods are quite similar to each other, except the enlarged portion (where the velocity profiles change sharply) shows that the result obtained by VISC-04 is the most satisfactory compared with the OpenFOAM results. It is also noticeable that OpenFOAM generally gives higher values of the velocity than ISPH for both the lid-driven flow and the lid-driven flow with an inside cylinder.

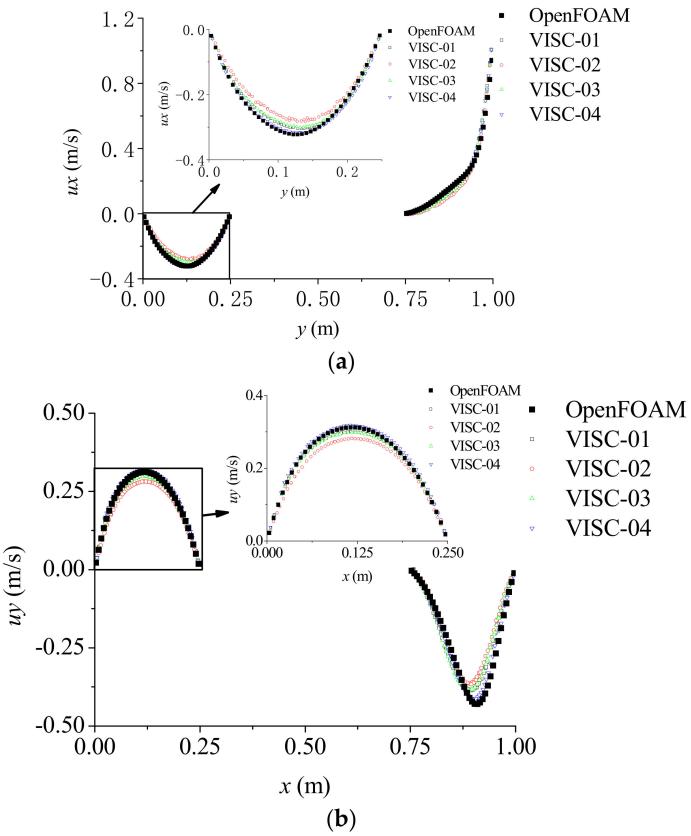

Figure 13. Comparisons of four viscosity force models for the lid-driven flow with an inside cylinder: (**a**) *ux* velocity distribution; and (**b**) *uy* velocity distribution.

For convergence and error analysis, Figure 14 gives the numerical errors of minimum velocity *ux* of various ISPH viscosity force models under different particle resolutions, where *Err* is defined as the same error used in the previous section. Again all the ISPH errors decrease with the deceasing particle size. In addition, it is also disclosed that the error of VISC-04 is the smallest, which is consistent with the conclusion drawn from Section 5.1.

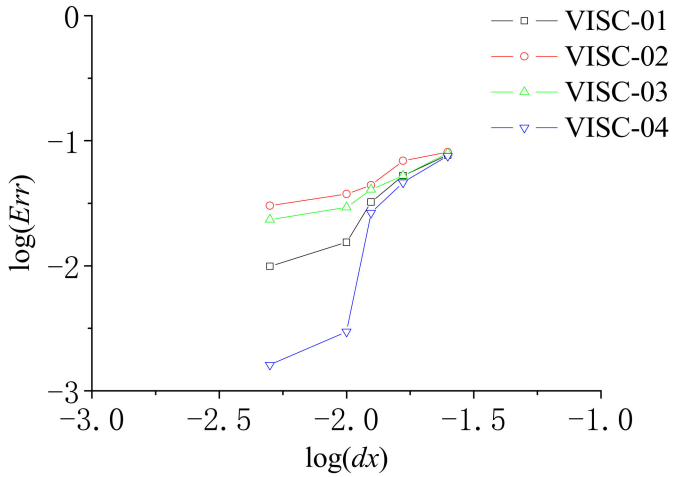

Figure 14. Convergence and error analysis of four viscosity force models for the different particle resolutions of a lid-driven flow with an inside cylinder.

6. Conclusions

For viscosity-dominated flow simulations, the viscous term in the N-S equations plays an important role. So an accurate treatment should be useful for fully exploring the great potentials of the mesh-free SPH method. One major difficulty arises from the fact that the viscosity term takes the form of a second-derivative and it is highly sensitive to the particle disorders. This work introduced a series of approaches to discretize the viscosity term and its main contributions lie in the following two aspects: firstly, by comparing with the formulations used to discretize the Laplacian of PPE, four benchmark calculation methods on the viscosity term were proposed; secondly, a comprehensive analysis on the different viscosity force models was carried out through vigorous benchmark tests, and the most accurate model was identified.

Contrary to the common feeling that a higher-accuracy discretized form can achieve the most accurate result, this should be carefully interpreted based on the different model applications. According to the model test on a polynomial function, VISC-03 was shown to achieve the highest accuracy under both the uniform and irregular particle distributions. However, as further disclosed in the subsequent practical model applications, such as a lid-driven flow, VISC-04 performed the most desirably instead. In nature, VISC-04 is improved from the fundamental framework of VISC-01 and just corrects the first-order derivative so as to achieve the maximum potentials. For all of the numerical tests, it is concluded that VISC-03 consumes the most CPU time, while VISC-02 is the fastest model although it may easily induce the instability under a disordered particle configuration. Generally speaking, although these four viscosity force models can all be used in the viscous flow simulations, it is recommended that VISC-04 has the highest accuracy, as least for the present case studies.

Although all the formulations discussed can be used for the practical free surface flow simulations in principle, it should be noted that the current study focuses a little more on the pure SPH numerical implementation technique, while the relevant underlying physics was not given sufficient attention. This should constitute our future research work.

Acknowledgments: This research work is supported by the National Natural Science Foundation of China (Nos. 51739001, 51579056, 51639004, 51379051 and 51479087), Foundational Research Funds for the Central Universities (Nos. HEUCDZ1202 and HEUCF170104), Defence Pre Research Funds Program (No. 9140A14020712CB01158) and Open Fund of the State Key Laboratory of Coastal and Offshore Engineering of Dalian University of Technology (LP1707). Author Qingwei Ma thanks the Chang Jiang Visiting Chair Professorship Scheme of the Chinese Ministry of Education, hosted by HEU. Author Songdong Shao thanks the Open Research Fund Program of the State Key Laboratory of Hydraulics and Mountain River Engineering, Sichuan University (No. SKHL1701).

Author Contributions: All authors contributed to the work. Xing Zheng performed the numerical computations and data analysis; Qingwei Ma guided the research work and edited/proof-read the paper; Songdong Shao drafted the manuscript and replied to the referees.

Conflicts of Interest: The authors declare no conflict of interest. The founding sponsors had no role in the design of the study; in the collection, analyses, or interpretation of data; in the writing of the manuscript, and in the decision to publish the results.

References

1. Bontozoglou, V. Laminar film flow along a periodic wall. *CMES* **2000**, *1*, 133–142.
2. Scholle, M.; Haas, A.; Aksel, N.; Wilson, M.C.T.; Thompson, M.C.T.; Gaskell, P.H. Competing geometric and inertial effects on local flow structure in thick gravity-driven fluid films. *Phys. Fluids* **2008**, *20*, 123101. [CrossRef]
3. Marner, F.; Gaskell, P.H.; Scholle, M. On a potential-velocity formulation of Navier-Stokes equations. *Phys. Mesomech.* **2014**, *17*, 341–348. [CrossRef]
4. Marner, F.; Gaskell, P.H.; Scholle, M. A complex-valued first integral of Navier-Stokes equations: Unsteady Couette flow in a corrugated channel system. *J. Math. Phys.* **2017**, *58*, 1127–1148. [CrossRef]
5. Monaghan, J.J. Simulating free surface flows with SPH. *J. Comput. Phys.* **1994**, *110*, 399–406. [CrossRef]
6. Khayyer, A.; Gotoh, H. On particle-based simulation of a dam break over a wet bed. *J. Hydraul. Res.* **2010**, *48*, 238–249. [CrossRef]
7. Gomez-Gesteira, M.; Cerqueiro, D.; Crespo, C.; Dalrymple, R.A. Green water overtopping analyzed with a SPH model. *Ocean Eng.* **2005**, *32*, 223–238. [CrossRef]
8. Federico, I.; Marrone, S.; Colagrossi, A.; Aristodemo, F.; Antuono, M. Simulating 2D open-channel flows through an SPH model. *Eur. J. Mech. B/Fluids* **2012**, *34*, 35–46. [CrossRef]
9. Ren, B.; Wen, H.; Dong, P.; Wang, Y. Numerical simulation of wave interaction with porous structures using an improved smoothed particle hydrodynamic method. *Coast. Eng.* **2014**, *88*, 88–100. [CrossRef]
10. Hu, X.Y.; Adams, N.A. An incompressible multi-phase SPH method. *J. Comput. Phys.* **2007**, *227*, 264–278. [CrossRef]
11. Chang, T.J.; Kao, H.M.; Chang, K.H.; Hsu, M.H. Numerical simulation of shallow-water dam break flows in open channels using smoothed particle hydrodynamics. *J. Hydrol.* **2011**, *408*, 78–90. [CrossRef]
12. Vacondio, R.; Rogers, B.D.; Stansby, P.K. Accurate particle splitting for smoothed particle hydrodynamics in shallow water with shock capturing. *Int. J. Numer. Methods Fluids* **2012**, *69*, 1377–1410. [CrossRef]
13. Shi, C.; An, Y.; Wu, Q.; Liu, Q.; Cao, Z. Numerical simulation of landslide-generated waves using a soil–water coupling smoothed particle hydrodynamics model. *Adv. Water Resour.* **2016**, *92*, 130–141. [CrossRef]
14. Pahar, G.; Dhar, A. Coupled incompressible Smoothed Particle Hydrodynamics model for continuum-based modelling sediment transport. *Adv. Water Resour.* **2017**, *102*, 84–98. [CrossRef]
15. Pahar, G.; Dhar, A. On modification of pressure gradient operator in integrated ISPH for multifluid and porous media flow with free-surface. *Eng. Anal. Bound. Elements* **2017**, *80*, 38–48. [CrossRef]
16. Meringolo, D.D.; Colagrossi, A.; Marrone, S.; Aristodemo, F. On the filtering of acoustic components in weakly-compressible SPH simulations. *J. Fluids Struct.* **2017**, *70*, 1–23. [CrossRef]
17. Aristodemo, F.; Tripepi, G.; Meringolo, D.D.; Veltri, P. Solitary wave-induced forces on horizontal circular cylinders: Laboratory experiments and SPH simulations. *Coast. Eng.* **2017**, *129*, 17–35. [CrossRef]
18. Antuono, M.; Colagrossi, A.; Marrone, S.; Molteni, D. Free-surface flows solved by means of SPH schemes with numerical diffusive terms. *Comput. Phys. Commun.* **2010**, *181*, 532–549. [CrossRef]
19. Zheng, X.; Shao, S.D.; Khayyer, A.; Duan, W.Y.; Ma, Q.W.; Liao, K.P. Corrected first-order derivative ISPH in water wave simulations. *Coast. Eng. J.* **2017**, *59*, 1750010. [CrossRef]
20. Colagrossi, A.; Landrini, M. Numerical simulation of interfacial flows by Smoothed Particle Hydrodynamics. *J. Comput. Phys.* **2003**, *191*, 448–475. [CrossRef]
21. Chen, Z.; Zong, Z.; Liu, M.B.; Li, H.T. A comparative study of truly incompressible and weakly compressible SPH methods for free surface incompressible flows. *Int. J. Numer. Methods Fluids* **2013**, *73*, 813–829. [CrossRef]
22. De Padova, D.; Dalrymple, R.A.; Mossa, M. Analysis of the artificial viscosity in the smoothed particle hydrodynamics modelling of regular waves. *J. Hydraul. Res.* **2014**, *52*, 836–848. [CrossRef]
23. Cummins, S.J.; Rudman, M. An SPH projection method. *J. Comput. Phys.* **1999**, *152*, 584–607. [CrossRef]

24. Shao, S.D.; Lo, E.Y.M. Incompressible SPH method for simulating Newtonian and non-Newtonian flows with a free surface. *Adv. Water Resour.* **2003**, *26*, 787–800. [CrossRef]
25. Morris, J.P.; Fox, P.J.; Zhu, Y. Modeling low Reynolds number incompressible flows using SPH. *J. Comput. Phys.* **1997**, *136*, 214–226. [CrossRef]
26. Khayyer, A.; Gotoh, H.; Shao, S.D. Corrected incompressible SPH method for accurate water-surface tracking in breaking waves. *Coast. Eng.* **2008**, *55*, 236–250. [CrossRef]
27. Gotoh, H.; Shibahara, T.; Sakai, T. Sub-particle-scale turbulence model for the MPS method—Lagrangian flow model for hydraulic engineering. *Comput. Fluid Dyn. J.* **2001**, *9*, 339–347.
28. Basa, M.; Quinlan, N.; Lastiwka, M. Robustness and accuracy of SPH formulations for viscous flow. *Int. J. Numer. Methods Fluids* **2009**, *60*, 1127–1148. [CrossRef]
29. Colagrossi, A.; Antuono, M.; Souto-Iglesias, A.; Le Touze, D. Theoretical analysis and numerical verification of the consistency of viscous smoothed-particle-hydrodynamics formulations in simulating free-surface flows. *Phys. Rev. E* **2011**, *84*, 026705. [CrossRef] [PubMed]
30. Grenier, N.; Le Touze, D.; Colagrossi, A.; Antuono, M.; Colicchio, G. Viscous bubbly flows simulation with an interface SPH model. *Ocean Eng.* **2013**, *69*, 88–102. [CrossRef]
31. Liu, Z.G.; Liu, Z.X. The comparison of viscous force approximations of Smoothed Particle Hydrodynamics in Poiseuille flow simulation. *J. Fluids Eng. (Trans. ASME)* **2017**, *139*, 051302. [CrossRef]
32. Ma, Q.W.; Zhou, Y.; Yan, S. A review on approaches to solving Poisson's equation in projection-based meshless methods for modelling strongly nonlinear water waves. *J. Ocean Eng. Mar. Energy* **2016**, *2*, 279–299. [CrossRef]
33. Zheng, X.; Ma, Q.W.; Duan, W.Y. Incompressible SPH method based on Rankine source solution for violent water wave simulation. *J. Comput. Phys.* **2014**, *276*, 291–314. [CrossRef]
34. Gotoh, H.; Khayyer, A.; Ikaria, H.; Arikawa, T.; Shimosak, K. On enhancement of incompressible SPH method for simulation of violent sloshing flows. *Appl. Ocean Res.* **2014**, *46*, 104–115. [CrossRef]
35. Schwaiger, H.F. An implicit corrected SPH formulation for thermal diffusion with linear free surface boundary conditions. *Int. J. Numer. Methods Eng.* **2008**, *75*, 647–671. [CrossRef]
36. Jian, W.; Liang, D.; Shao, S.; Chen, R.; Yang, K. Smoothed Particle Hydrodynamics simulations of dam-Break flows around movable structures. *Int. J. Off. Polar Eng.* **2016**, *26*, 33–40. [CrossRef]
37. Oger, G.; Doring, M.; Alessandrini, B.; Ferrant, P. An improved SPH method: Towards higher order convergence. *J. Comput. Phys.* **2007**, *225*, 1472–1492. [CrossRef]
38. Hosseini, S.M.; Feng, J.J. Pressure boundary conditions for computing incompressible flows with SPH. *J. Comput. Phys.* **2011**, *230*, 7473–7487. [CrossRef]
39. Leroy, A.; Violeau, D.; Ferrand, M.; Kassiotis, C. Unified semi-analytical wall boundary conditions applied to 2-D incompressible SPH. *J. Comput. Phys.* **2014**, *261*, 106–129. [CrossRef]
40. Aly, A.M.; Asai, M.; Chamkha, A.J. Analysis of unsteady mixed convection in lid-driven cavity included circular cylinders motion using an incompressible smoothed particle hydrodynamics method. *Int. J. Numer. Methods Heat Fluid Flow* **2015**, *25*, 2000–2021. [CrossRef]
41. Yildiz, M.; Rook, R.A.; Suleman, A. SPH with the multiple boundary tangent method. *Int. J. Numer. Methods Eng.* **2009**, *77*, 1416–1438. [CrossRef]
42. Weller, H.G.; Tabor, G.; Jasak, H.; Fureby, C. A tensorial approach to computational continuum mechanics using object-oriented techniques. *Comput. Phys.* **1998**, *12*, 620–631. [CrossRef]
43. Ghia, U.; Ghia, K.N.; Shin, C.T. High-Re solutions for incompressible flow using the Navier-Stokes equations and a multigrid method. *J. Comput. Phys.* **1982**, *48*, 387–411. [CrossRef]